Available online at www.sciencedirect.com
ScienceDirect
Comput. Methods Appl. Mech. Engrg. 357 (2019) 112596
Computer methods in applied mechanics and engineering
www.elsevier.com/locate/cma

Continuous data assimilation reduced order models of fluid flow

Camille Zerfas[a,1], Leo G. Rebholz[a,1], Michael Schneier[b,*], Traian Iliescu[c,2]

[a] Department of Mathematical Sciences, Clemson University, Clemson, SC, 29634, United States of America
[b] Department of Mathematics, University of Pittsburgh, Pittsburgh, PA, 15213, United States of America
[c] Department of Mathematics, Virginia Tech, Blacksburg, VA, 24061, United States of America

Received 10 March 2019; received in revised form 8 August 2019; accepted 11 August 2019
Available online xxxx

Highlights

- Incorporate nudging based data assimilation into a reduced order modeling framework.
- Prove that the new DA-ROM converges exponentially fast in time to the true solution.
- Demonstrate that the DA-ROM strategy can provide long time accuracy in ROMs.

Abstract

We propose, analyze, and test a novel continuous data assimilation reduced order model (DA-ROM) for simulating incompressible flows. While ROMs have a long history of success on certain problems with recurring dominant structures, they tend to lose accuracy on more complicated problems and over longer time intervals. Meanwhile, continuous data assimilation (DA) has recently been used to improve accuracy and, in particular, long time accuracy in fluid simulations by incorporating measurement data into the simulation. This paper synthesizes these two ideas, in an attempt to address inaccuracies in ROM by applying DA, especially over long time intervals and when only inaccurate snapshots are available. We prove that with a properly chosen nudging parameter, the proposed DA-ROM algorithm converges exponentially fast in time to the true solution, up to discretization and ROM truncation errors. Finally, we propose a strategy for nudging adaptively in time, by adjusting dissipation arising from the nudging term to better match true solution energy. Numerical tests confirm all results, and show that the DA-ROM strategy with adaptive nudging can be highly effective at providing long time accuracy in ROMs.
© 2019 Elsevier B.V. All rights reserved.

Keywords: Navier–stokes equations; Proper orthogonal decomposition; Data assimilation; Reduced order modeling

1. Introduction

Reduced order models (ROMs) for fluids dominated by relatively few recurrent spatial structures are generally built as follows [1–3]: (i) postulate a collection of snapshots, either from numerical experiments or from physical data; (ii) from those snapshots, select a small number (e.g., 10) of ROM basis functions; (iii) project the equations

* Corresponding author.
E-mail addresses: czerfas@clemson.edu (C. Zerfas), rebholz@clemson.edu (L.G. Rebholz), mhs64@pitt.edu (M. Schneier), iliescu@vt.edu (T. Iliescu).

[1] This author was partially supported by NSF Grant DMS 1522191.
[2] This author was partially supported by NSF Grant DMS 1821145.

https://doi.org/10.1016/j.cma.2019.112596
0045-7825/© 2019 Elsevier B.V. All rights reserved.

of motion into this basis; and (iv) advance the velocity in time to interrogate flows different from the one generating the snapshots. ROMs have been explored for decades [2]. When successful, ROMs can decrease the computational cost of a brute force, direct numerical simulation (DNS) by orders of magnitude.

One of the main roadblocks for ROMs of realistic flows is their *lack of accuracy*, e.g., in complex problems, for long time intervals, or when a low-dimensional ROM basis is used. To increase the ROM accuracy in practical applications, several approaches are currently used. We list some of these below:

(i) Closure Modeling: To model the effect of the discarded ROM modes, a *Correction* term is generally added to the standard ROM [4–7]. Given the drastic truncation used in ROMs for realistic flows, the Correction term is essential for accuracy.

(ii) Numerical Stabilization: To eliminate/alleviate the spurious numerical oscillations generated when ROMs are used for convection-dominated flows, numerical stabilization techniques can be used [7–9].

(iii) Data-Driven Modeling: Recently, available numerical or experimental data have been used to construct ROM operators [10] or to determine the unknown coefficients in classical ROM operators [4,6,11].

(iv) Improved Basis: Another approach for increasing the ROM accuracy in practical applications is the construction of an improved (more accurate) ROM basis that better captures the behavior of the underlying system [12–15].

(v) Physical Accuracy: To develop physically sound ROMs, recent effort has been directed at ensuring that the ROMs *satisfy the same physical balances/conservation laws* as those satisfied by the equations of motion [16,17].

In this paper, we propose to increase the ROM accuracy through the use of *data assimilation (DA)*, and in particular we use a type of DA recently introduced by Azouani et al. [18] called continuous data assimilation to create a novel DA-ROM. In weather modeling, climate science, and hydrological and environmental forecasting, DA has been used for decades to incorporate observational data in simulations, in order to increase the accuracy of solutions and to obtain better estimates of initial conditions [19]. Continuous data assimilation has recently become popular due to a seminal paper of Azouani et al. [18], and since then it has been used to improve solutions to many different types of evolutionary systems including for Navier–Stokes simulations [20], with noisy data [21], with nudging applied to only one component [22], from a numerical viewpoint [23], for multiphysics fluid problems [24,25], surface quasi-geostrophic simulations [26], and a generalization to types of transient nonlinear systems [27].

In this paper, we use DA to improve the ROM accuracy, complete with mathematical proof. Specifically, we add to the standard ROM a feedback control term of the form

$$\mu\, I_H(u_r - u_{obs}), \tag{1.1}$$

which nudges the ROM approximation (u_r) towards the reference solution (u_{obs}) corresponding to the observed data. We note that although the DA terminology is 'nudging', one can also consider it as a penalization of the solution so that its interpolant better matches the measurement data (i.e., the interpolant of the true solution).

In (1.1), I_H is an interpolation operator onto a coarser mesh of size H and $\mu > 0$ is a nudging parameter. The nudging term (1.1) increases the accuracy of the new DA-ROM by utilizing the available low-resolution data, without the need to increase the number of ROM basis functions. Two key components of the nudging term are that it allows the *simple* implementation of DA into existing ROM codes, and moreover, permits us to prove herein that the DA-ROM solution will converge to the true solution, exponentially fast in time, up to discretization and ROM truncation errors (such results are seemingly unavailable for other types of DA). In addition to these key features of the DA we apply herein, the intent of this DA is also different from other uses of DA for ROMs, e.g., [28–31]: In the latter the authors use ROMs to *speed up classical DA algorithms* (e.g., 4D-VAR), whereas the DA-ROM proposed in this paper is intended to *improve the ROM accuracy*.

The rest of the paper is organized as follows: In Section 2, we introduce some notation and preliminaries necessary for our analysis. In Section 3, we construct the new DA-ROM and perform a careful error analysis. In Section 4, we perform a numerical investigation of the new DA-ROM in the numerical simulation of a 2D flow past a circular cylinder and discuss implementation of the DA-ROM algorithm with an adaptive nudging parameter, which can be used to further improve the accuracy of solutions. Finally, in Section 5, we draw conclusions and outline future research directions.

2. Notation and preliminaries

Let $\Omega \subset \mathbb{R}^d$, $d = 2$ or 3, be a bounded open domain. The $L^2(\Omega)$ norm and inner product will be denoted by $\|\cdot\|$ and $(\cdot,\cdot)$, respectively, and all other norms will be appropriately labeled with subscripts.

We consider the *Navier–Stokes equations (NSE)* with no-slip boundary conditions:

$$\begin{aligned} &u_t + u\cdot\nabla u + \nabla p - \nu\Delta u = f, \text{ and } \nabla\cdot u = 0, \text{ in } \Omega\times(0,T] \\ &u = 0, \text{ on } \partial\Omega\times(0,T], \text{ and } u(x,0) = u_0(x), \text{ in } \Omega. \end{aligned} \tag{2.1}$$

Here u is the velocity, $f = f(x,t)$ is the known body force, p is the pressure, and ν is the kinematic viscosity.

We denote the natural velocity space by $X = H_0^1(\Omega)^d$ and pressure space by $Q = L_0^2(\Omega)$ and by $(X_h, Q_h) \subset (X, Q)$, corresponding inf–sup stable finite element (FE) spaces. We assume herein that $(X_h, Q_h) = (\mathcal{P}_k, \mathcal{P}_{k-1})$ finite elements, either Taylor–Hood or Scott–Vogelius on appropriate meshes. In our computations, $k = 2$.

Additionally, we define the discretely divergence-free space V_h as

$$V_h := \{v_h \in X_h \,:\, (\nabla\cdot v_h, q_h) = 0 \ \forall q_h \in Q_h\} \subset X.$$

The Poincaré inequality will be used throughout this paper: there exists a constant C_P depending only on Ω such that

$$\|\phi\| \le C_P\|\nabla\phi\| \ \forall\phi \in X.$$

We define the trilinear form

$$b(w,u,v) = (w\cdot\nabla u, v) \qquad \forall u, v, w \in X,$$

and the explicitly skew-symmetric trilinear form given by

$$b^*(w,u,v) := \frac{1}{2}(w\cdot\nabla u, v) - \frac{1}{2}(w\cdot\nabla v, u) \qquad \forall u, v, w \in X\,.$$

An important property of the b^* operator is that $b^*(u,v,v) = 0$ for $u, v \in X$. We will utilize the following bound on the operator b^* from Lemma 6.14 of [32].

Lemma 2.2. *Let $u, v, w \in X$ and let $s \in (0,1]$ if $d = 2$ and $s \in [1/2, 1]$ if $d = 3$. There exists a constant $C_b > 0$ dependent only on Ω and s satisfying*

$$|b^*(u,v,w)| \le C_b\|u\|^{1-s}\|\nabla u\|^s\|\nabla v\|\|\nabla w\|.$$

The following lemma is proven in [23], and is useful in our analysis.

Lemma 2.3. *Suppose constants r and B satisfy $r > 1$, $B \ge 0$. Then, if the sequence of real numbers $\{a_n\}$ satisfies*

$$ra_{n+1} \le a_n + B, \tag{2.4}$$

we have that

$$a_{n+1} \le a_0\left(\frac{1}{r}\right)^{n+1} + \frac{B}{r-1}.$$

In order to construct a ROM, in the ensuing section we will consider a full order model based on a FE discretization of (2.1). We let $t^n = n\Delta t$, $n = 0, 1, 2, \ldots, M$, where $M := T/\Delta t$, denotes a partition of the interval $[0, T]$. We then consider the BDF2 time discretization with Taylor–Hood elements: Given initial conditions u^0 and u^1, let $u_h^0 = P_h u^0 \in X_h$ and $u_h^1 = P_h u^1 \in X_h$, where P_h denotes the L^2 projection into the FE space. Then, for $n = 1, 2, \ldots, M$, we find $u_h^{n+1} \in X_h$ and $p_h^{n+1} \in Q_h$ satisfying

$$\begin{aligned} \left(\frac{3u_h^{n+1} - 4u_h^n + u_h^{n-1}}{2\Delta t}, v_h\right) + \nu(\nabla u_h^{n+1}, \nabla v_h) + b^*(u_h^{n+1}, u_h^{n+1}, v_h) \\ -(p_h^{n+1}, \nabla\cdot v_h) = (f^{n+1}, v_h) \qquad \forall v_h \in X_h \\ (\nabla\cdot u_h^{n+1}, q_h) = 0 \qquad \forall q_h \in Q_h. \end{aligned} \tag{2.5}$$

2.1. ROM preliminaries

We define $Y = \{\hat{u}_h^1, \ldots, \hat{u}_h^M\}$ to be the snapshot matrix consisting of the basis coefficient vectors of the FE solutions $\{u_h^1, \ldots, u_h^M\}$ of (2.5) for M different time instances. The proper orthogonal decomposition (POD) seeks a low-dimensional basis that approximates these snapshots optimally with respect to a certain norm; in this paper, we use the L^2 norm. Let N_h denote the dimension of the FE velocity space and M_h the FE mass matrix. This minimization can be set up as an eigenvalue problem $YY^T M_h \omega_j = \lambda_j \omega_j$, $j = 1, \ldots, N_h$, where the eigenvalues are real and non-negative, so they can be ordered as $\lambda_1 \geq \cdots \geq \lambda_R \geq \lambda_{R+1} = \cdots = \lambda_{N_h} = 0$, where R is the rank of the snapshot matrix. The FE basis coefficients of the individual POD basis functions $\hat{\varphi}_i$ will then be given by

$$\hat{\varphi}_i = \frac{1}{\lambda_i} Y^T \omega_i, \qquad i = 1, \ldots, R.$$

Letting φ_i be the function corresponding to the coefficients $\hat{\varphi}_i$, we then take the ROM space to be $X_r := \text{span}\{\varphi_i\}_{i=1}^r$, where $r \leq R$, and note that since discrete FE solutions of the NSE are discretely divergence free, it follows that $X_r \subset V_h$. The ROM approximation of the velocity is defined as

$$u_r(x,t) = \sum_{j=1}^{r} a_j(t)\varphi_j(x),$$

where the coefficients $a_j(t)$ are determined by solving the Galerkin ROM (G-ROM):

$$(u_{r,t}, \varphi_i) + \nu(\nabla u_r, \nabla \varphi_i) + b^*(u_r, u_r, \varphi_i) = (f, \varphi_i). \tag{2.6}$$

We emphasize that, since $X_r \subset V_h$, the G-ROM (2.6) does not include a ROM pressure approximation. ROMs that include a pressure approximation are surveyed in, e.g., [1,3].

We define the L^2 ROM projection $P_r : L^2 \to X_r$ by: for all $v \in L^2(\Omega)$, $P_r(v)$ is the unique element of X_r such that

$$(P_r(v), v_r) = (v, v_r) \quad \forall\, v_r \in X_r. \tag{2.7}$$

Letting $\mathbb{S}_r = (\nabla \varphi_i, \nabla \varphi_j)$, $i, j = 1, \ldots, r$ denote the POD stiffness matrix, it can be shown that the following inverse inequality holds for our ROM basis [33].

Lemma 2.8 (*POD Inverse Estimate*)**.**

$$\|\nabla \varphi\| \leq |||\mathbb{S}_r|||_2^{1/2} \|\varphi\| \quad \forall \varphi \in X_r, \tag{2.9}$$

where $|||\mathbb{S}_r|||_2$ *is the matrix 2-norm of the ROM stiffness matrix.*

In order to establish an error estimate for the ROM projection, we first make the following assumption on the finite element error:

Assumption 2.10. Let $C(\nu, p)$ denote a constant which is dependent upon the viscosity and pressure. We assume that the finite element error u_h satisfies the following error estimate

$$\|u^M - u_h^M\|^2 + \nu h^2 \Delta t \sum_{n=1}^{M} \|\nabla(u^n - u_h^n)\|^2 \leq C(\nu, p)(h^{2k+2} + \Delta t^4). \tag{2.11}$$

Remark 2.12. Error estimates of this form have been proven for varying amounts of regularity on the continuous solution u and p. Some examples include the scheme used in the numerical experiments in Section 4.

Using Assumption 2.10, the following error estimates for the ROM projection can be proven [34]:

Lemma 2.13. *The* L^2 *ROM projection of* u^n *satisfies the following error estimates:*

$$\sum_{n=1}^{M} \|u^n - P_r(u^n)\|^2 \leq C(\nu, p)\left(h^{2k+2} + \Delta t^4 + \sum_{j=r+1}^{d} \lambda_j\right), \tag{2.14}$$

$$\sum_{n=1}^{M} \|\nabla(u^n - P_r(u^n))\|^2 \le C(\nu, p)\Bigg(h^{2k} + |||\mathbb{S}_R|||_2 h^{2k+2} + (1 + |||\mathbb{S}_R|||_2)\Delta t^4 + \sum_{j=r+1}^{d} \|\nabla\varphi_j\|^2 \lambda_j\Bigg). \tag{2.15}$$

We then make the following assumption similar to that made in [34,35]:

Assumption 2.16. The L^2 ROM projection of u^n satisfies the following error estimates:

$$\max_n \|u^n - P_r(u^n)\|^2 \le C(\nu, p)\Bigg((h^{2k+2} + \Delta t^4) + \sum_{j=r+1}^{d} \lambda_j\Bigg), \tag{2.17}$$

$$\max_n \|\nabla(u^n - P_r(u^n))\|^2 \le C(\nu, p)\Bigg(h^{2k} + |||\mathbb{S}_R|||_2 h^{2k+2} + (1 + |||\mathbb{S}_R|||_2)\Delta t^4 + \sum_{j=r+1}^{d} \|\nabla\varphi_j\|^2 \lambda_j\Bigg). \tag{2.18}$$

2.2. Data assimilation preliminaries

We consider I_H to be an interpolation operator that satisfies: For a given mesh $\tau_H(\Omega)$ with $H \le 1$,

$$\|I_H(w) - w\| \le C_I H \|\nabla w\|, \tag{2.19}$$

$$\|I_H(w)\| \le C_I \|w\|, \tag{2.20}$$

for any $w \in H^1(\Omega)$. For example, this holds for the L^2 projection onto piecewise constants, and the Scott–Zhang interpolant. For the (unknown) true solution u, $I_H(u)$ represents an approximation of what is observed of the true solution. We assume in this paper that $I_H(u)$ can be observed at any time.

3. Error analysis

For simplicity of exposition, our analysis considers a first order DA-ROM algorithm, which takes the following form: Find $u_r^{n+1} \in X_r$ such that for all $v_r \in X_r$,

$$\frac{1}{\Delta t}(u_r^{n+1} - u_r^n, v_r) + b^*(u_r^{n+1}, u_r^{n+1}, v_r) + \nu(\nabla u_r^{n+1}, \nabla v_r) + \mu(I_H(u_r^{n+1} - u(t^{n+1})), I_H v_r) = (f^{n+1}, v_r), \tag{3.1}$$

for $n = 1, 2, \ldots, M$, with the initial condition given by $u_r^0 = P_r(u_0)$, and where $\mu \ge 0$ is the nudging parameter. Extension to other time stepping methods is possible, and, for example, extension to BDF2 can be done following the usual techniques [23]. All of our numerical tests use the analogous BDF2 algorithm.

The nudging used above is $\mu(I_H(u_r^{n+1} - u(t^{n+1})), I_H v_r)$, which differs from the usual continuous DA nudging in that interpolation is also applied to the test function v_r. This was originally suggested in [36], and since also used in [37,38]. As shown in [36] and below, using this nudging term does not affect convergence analysis; some extra terms arise that can be handled without difficulty. However, this term does provide for simple unconditional convergence, without any data restrictions, since choosing $v_r = u_r^{n+1}$ in the nudging term produces

$$\mu(I_H(u_r^{n+1} - u(t^{n+1})), I_H u_r^{n+1}) = \frac{\mu}{2}\left(\|I_H u_r^{n+1}\|^2 - \|I_H u(t^{n+1})\|^2 + \|I_H(u_r^{n+1} - u(t^{n+1}))\|^2\right). \tag{3.2}$$

Combining this with usual ROM stability analysis for NSE yields the following stability lemma:

Lemma 3.3. *The solutions to (3.1) satisfy for all $M > 1$,*

$$\|u_r^M\|^2 \le \|u_r^0\|^2 \left(\frac{1}{1 + \lambda\Delta t}\right)^M + C\lambda^{-1}(\nu^{-1}F^2 + \mu U^2) := C_{data},$$

where $F := \|f\|_{L^\infty(0,\infty;H^{-1})}$, $U := \|u\|_{L^\infty(0,\infty;L^2)}$, and $\lambda = \nu C_P^{-2}$.

Proof. This result follows as in [23] by letting $v_r = u_r^{n+1}$ in (3.1) and using Cauchy–Schwarz and Young's inequalities, along with (3.2). The non-negative DA term $\|I_H u_r^{n+1}\|^2$ can be dropped from the left after bounding the right hand side. □

To analyze rates of convergence of the approximation, we make the following regularity assumptions on the NSE [39]:

Assumption 3.4. We assume that the solution of the NSE satisfies

$$u \in L^\infty(0,T;H^1(\Omega)) \cap H^1(0,T;H^{k+1}(\Omega)) \cap H^2(0,T;H^1(\Omega)),$$
$$p \in L^2(0,T;H^{k+1}(\Omega)),$$
$$f \in L^2(0,T;L^2(\Omega)).$$

Here, k comes from the finite element spaces being $(\mathcal{P}_k, \mathcal{P}_{k-1})$ for velocity–pressure. In our computations, $k = 2$. These are strong assumptions, which may not be true for all flows, and represent a best case scenario for solution regularity.

We next prove that solutions to (3.1) converge to the true solution exponentially fast, up to discretization and ROM projection error.

Theorem 3.5. *Define*

$$\alpha_1 := \nu - 2\mu(\beta_2 - 1)C_I^2 H^2,$$
$$\alpha_2 := 2\mu - \frac{\mu C_I^2}{2\beta_1} - \frac{\mu}{2\beta_2} - 6\nu^{-1}{C_b}^2 |||\mathbb{S}_r|||_2 \|\nabla u^{n+1}\|^2,$$

which have parameters μ, H, $\beta_i > 0$, $i = 1, 2$ that are chosen so that $\alpha_i > 0$, $i = 1, 2$. Then under the regularity conditions of Assumption 3.4, we have that

$$\begin{aligned} \| u^{n+1} - u_r^{n+1} \|^2 \leq \|u^0 - u_r^0\|^2 &\left(\frac{1}{1+2\lambda\Delta t}\right)^{n+1} \\ &+ C\lambda^{-1}\left\{ \nu^{-1}\Delta t^2 + \nu^{-1}h^{2k} + \beta_1 C_I^2 \mu\left(h^{2k+2} + \Delta t^4 + \sum_{j=r+1}^{d} \lambda_j\right)\right. \\ &\left. + (\nu^{-1}{C_b}^2 + \nu^{-1}{C_b}^2 |||\mathbb{S}_r|||_2)\left(h^{2k} + \Delta t^4 + \sum_{j=r+1}^{d} \|\nabla\varphi_j\|^2 \lambda_j\right)\right\}, \end{aligned} \tag{3.6}$$

where $\lambda = \min\{\alpha_1 C_P^{-2}, \alpha_2\}$.

Remark 3.7. The Δt^2 term that shows up on the right hand side of (3.6) is a result of the first order time stepping in (3.1). If we instead used a second order approximation, like BDF2, then this term would be replaced by Δt^4.

Remark 3.8. The use of β_i's and α_i's improves on the usual restriction of the relationship between H, ν, and μ, i.e., that $\nu - 2\mu C_I^2 H^2 > 0$ (see e.g. [23] and references therein). It reveals that this usual restriction can be relaxed, or even eliminated, but at the cost of increasing the error bound: smaller β_2 creates a larger β_1, and β_1 scales the (potentially large) error term $\mu \sum_{j=r+1}^{d} \lambda_j$ in the error bound. Furthermore, we note that, as shown in Remark 3.3 in [40], $|||\mathbb{S}_r|||_2$ increases when r increases. Thus, for fixed β_i, to enforce $\alpha_2 > 0$, one needs relatively large μ values, which in turn increases the error bound. The practical value from this result is likely more heuristic than sharp, since improvements in upper bounds on error do not always translate to better results in a particular setting (where a dominant error source can mask other error sources). However, our bounds clearly show that using smaller H improves the error bound, which is not surprising since taking small H corresponds to having more observational data.

Proof. The NSE (true) solution satisfies

$$\frac{1}{\Delta t}(u^{n+1}-u^n, v_r) + b^*(u^{n+1},u^{n+1}, v_r) + \nu(\nabla u^{n+1}, \nabla v_r) + (p^{n+1}, \nabla\cdot v_r) = (f^{n+1}, v_r) + \tau_u(u^{n+1}; v_r), \tag{3.9}$$

where

$$\tau_u(u^{n+1}; v_r) = \left(\frac{u^{n+1}-u^n}{\Delta t} - u_t(t^{n+1}), v_r\right). \tag{3.10}$$

Subtracting (3.1) from (3.9) and letting $e^n := u_r^n - u^n$, we obtain

$$\frac{1}{\Delta t}(e^{n+1}-e^n, v_r) + \nu(\nabla e^{n+1}, \nabla v_r) + \mu(I_H e^{n+1}, I_H v_r) = \tau_u(u^{n+1}; v_r) + b^*(u_r^{n+1}, e^{n+1}, v_r) + b^*(e^{n+1}, u^{n+1}, v_r) + (p^{n+1}, \nabla\cdot v_r). \tag{3.11}$$

Decompose the error as a part inside the ROM space and one outside by adding and subtracting the L^2 projection of u^n into the ROM space, $P_r(u^n)$ (see (2.7)):

$$e^n = (u_r^n - P_r(u^n)) + (P_r(u^n) - u^n) =: \phi_r^n + \eta^n.$$

Letting $v_r = \phi_r^{n+1}$ in (3.11), we note that since $\phi_r^{n+1} \in X_r \subset V_h$, for any $q_h \in Q_h$,

$$(p^{n+1}, \nabla\cdot\phi_r^{n+1}) = (p^{n+1} - q_h, \nabla\cdot\phi_r^{n+1}). \tag{3.12}$$

Adding and subtracting ϕ_r^{n+1} to both components of the nudging term we have

$$\begin{aligned}
&(I_H\phi_r^{n+1} + I_H\eta^{n+1} + \phi_r^{n+1} - \phi_r^{n+1}, I_H\phi_r^{n+1} + \phi_r^{n+1} - \phi_r^{n+1})\\
&= \|\phi_r^{n+1}\|^2 + (\phi_r^{n+1}, I_H\phi_r^{n+1} - \phi_r^{n+1}) + (I_H\phi_r^{n+1} + I_H\eta^{n+1} - \phi_r^{n+1}, I_H\phi_r^{n+1} + \phi_r^{n+1} - \phi_r^{n+1})\\
&= \|\phi_r^{n+1}\|^2 + (\phi_r^{n+1}, I_H\phi_r^{n+1} - \phi_r^{n+1}) + (I_H\eta^{n+1}, I_H\phi_r^{n+1} + \phi_r^{n+1} - \phi_r^{n+1})\\
&+ (I_H\phi_r^{n+1} - \phi_r^{n+1}, I_H\phi_r^{n+1} - \phi_r^{n+1} + \phi_r^{n+1})\\
&= \|\phi_r^{n+1}\|^2 + 2(\phi_r^{n+1}, I_H\phi_r^{n+1} - \phi_r^{n+1}) + (I_H\eta^{n+1}, I_H\phi_r^{n+1}) + \|I_H\phi_r^{n+1} - \phi_r^{n+1}\|^2.
\end{aligned} \tag{3.13}$$

Using the polarization identity on the term $(\phi_r^{n+1} - \phi_r^n, \phi_r^{n+1})$, the fact that $(\eta^{n+1} - \eta^n, \phi_r^{n+1}) = 0$ (by the definition of the L^2 projection), and dropping the nonnegative term $\frac{1}{2\Delta t}\|\phi_r^{n+1} - \phi_r^n\|^2$ on the left hand side, we have

$$\begin{aligned}
&\frac{1}{2\Delta t}[\|\phi_r^{n+1}\|^2 - \|\phi_r^n\|^2] + \nu\|\nabla\phi_r^{n+1}\|^2 + \mu\|\phi_r^{n+1}\|^2 + \mu\|I_H\phi_r^{n+1} - \phi_r^{n+1}\|^2\\
&\quad\le \nu|(\nabla\eta^{n+1}, \nabla\phi_r^{n+1})| + \left|\tau_u(u^{n+1}; \phi_r^{n+1})\right| + |b^*(u_r^{n+1}, \eta^{n+1}, \phi_r^{n+1})|\\
&\qquad + |b^*(\eta^{n+1}, u^{n+1}, \phi_r^{n+1})| + |b^*(\phi_r^{n+1}, u^{n+1}, \phi_r^{n+1})| + |(p^{n+1} - q_h, \nabla\cdot\phi_r^{n+1})|\\
&\qquad + \mu|(I_H\eta^{n+1}, I_H\phi_r^{n+1})| + 2\mu|(\phi_r^{n+1}, I_H\phi_r^{n+1} - \phi_r^{n+1})|.
\end{aligned} \tag{3.14}$$

By Poincaré, Cauchy–Schwarz, and Young's inequalities, we bound the first term on the right hand side and the pressure term,

$$\begin{aligned}
\nu(\nabla\eta^{n+1}, \nabla\phi_r^{n+1}) &\le \frac{\nu}{4c_1}\|\nabla\eta^{n+1}\|^2 + c_1\nu\|\nabla\phi_r^{n+1}\|^2,\\
(p^{n+1} - q_h, \nabla\cdot\phi_r^{n+1}) &\le \frac{\nu^{-1}}{4c_2}\|p^{n+1} - q_h^{n+1}\|^2 + c_2\nu\|\nabla\phi_r^{n+1}\|^2.
\end{aligned} \tag{3.15}$$

We then bound the consistency term using Taylor's theorem (see Lemma 7.67 of [32]), and Poincaré, Cauchy–Schwarz, and Young's inequalities:

$$\begin{aligned}
\left|\tau_u(u^{n+1}; \phi_r^{n+1})\right| &\le \left\|\frac{u^{n+1}-u^n}{\Delta t} - u_t(t^{n+1})\right\|\|\phi_r^{n+1}\|\\
&\le \frac{CC_P^2\Delta t^2\nu^{-1}}{4c_3}\|u_{tt}\|^2_{L^2(t_n, t_{n+1}; L^2(\Omega))} + c_3\nu\|\nabla\phi_r^{n+1}\|^2.
\end{aligned} \tag{3.16}$$

The first two nonlinear terms are now bounded similarly to those in [17] using Cauchy–Schwarz and Young's inequalities, and the first inequality from Lemma 2.2 with $s = 1$:

$$b^*(\eta^{n+1}, u^{n+1}, \phi_r^{n+1}) \leq \frac{\nu^{-1}{C_b}^2}{4c_4}\|\nabla u^{n+1}\|^2\|\nabla\eta^{n+1}\|^2 + c_4\nu\|\nabla\phi_r^{n+1}\|^2, \tag{3.17}$$

$$b^*(u_r^{n+1}, \eta^{n+1}, \phi_r^{n+1}) \leq \frac{\nu^{-1}{C_b}^2}{4c_5}\|\nabla u_r^{n+1}\|^2\|\nabla\eta^{n+1}\|^2 + c_5\nu\|\nabla\phi_r^{n+1}\|^2. \tag{3.18}$$

How we treat the third nonlinear term is the key difference in the proof from standard schemes (see chapter 9 of [39]). Due to the added dissipation from the DA term on the left-hand side of (3.14), we are able to hide the term containing ϕ_r^{n+1}, rather than invoking a discrete Gronwall's inequality. Thus, for this term we use Lemma 2.2 with $s = \frac{1}{2}$ and the ROM inverse inequality (2.9) to obtain

$$\begin{aligned} b^*(\phi_r^{n+1}, u^{n+1}, \phi_r^{n+1}) &\leq C_b\|\phi_r^{n+1}\|^{1/2}\|\nabla\phi_r^{n+1}\|^{1/2}\|\nabla u^{n+1}\|\|\nabla\phi_r^{n+1}\| \\ &\leq \frac{\nu^{-1}{C_b}^2|||\mathbb{S}_r|||_2}{4c_6}\|\nabla u^{n+1}\|^2\|\phi_r^{n+1}\|^2 + c_6\nu\|\nabla\phi_r^{n+1}\|^2. \end{aligned} \tag{3.19}$$

The first nudging terms on the right hand side of (3.14) are bounded using (2.20), Cauchy–Schwarz, and Young's inequality

$$\begin{aligned} \mu(I_H\eta^{n+1}, I_H\phi_r^{n+1}) &\leq \frac{\mu}{4\beta_1}\|I_H\phi_r^{n+1}\|^2 + \mu\beta_1\|I_H\eta^{n+1}\|^2 \\ &\leq \frac{\mu C_I^2}{2\beta_1}\|\phi_r^{n+1}\|^2 + 2\mu\beta_1 C_I^2\|\eta^{n+1}\|^2. \end{aligned} \tag{3.20}$$

The second nudging term is bounded using Cauchy–Schwarz and Young's inequality, and (2.19), yielding

$$\begin{aligned} 2\mu(\phi_r^{n+1}, I_H\phi_r^{n+1} - \phi_r^{n+1}) &\leq \frac{\mu}{4\beta_2}\|\phi_r^{n+1}\|^2 + \mu\beta_2\|I_H\phi_r^{n+1} - \phi_r^{n+1}\|^2 \\ &= \frac{\mu}{4\beta_2}\|\phi_r^{n+1}\|^2 + \mu(\beta_2 - 1)\|I_H\phi_r^{n+1} - \phi_r^{n+1}\|^2 + \mu\|I_H\phi_r^{n+1} - \phi_r^{n+1}\|^2 \\ &\leq \frac{\mu}{4\beta_2}\|\phi_r^{n+1}\|^2 + C_I^2H^2\mu(\beta_2 - 1)\|\nabla\phi_r^{n+1}\|^2 + \mu\|I_H\phi_r^{n+1} - \phi_r^{n+1}\|^2. \end{aligned} \tag{3.21}$$

Now letting $c_i = \frac{1}{12}$, $i = 1, 2, \ldots, 6$, combining terms, and recalling our definition of α_1 and α_2 given in the statement of the theorem, (3.14) becomes

$$\begin{aligned} &\|\phi_r^{n+1}\|^2 + \alpha_1\Delta t\|\nabla\phi_r^{n+1}\|^2 + \alpha_2\Delta t\|\phi_r^{n+1}\|^2 \\ &\quad\leq \|\phi_r^n\|^2 + C\Delta t^3\nu^{-1}\|u_{tt}\|^2_{L^2(t_n,t_{n+1};L^2(\Omega))} + C\Delta t\nu^{-1}{C_b}^2\|\nabla\eta^{n+1}\|^2\|\nabla u^{n+1}\|^2 \\ &\quad+ C\Delta t\nu^{-1}{C_b}^2\|\nabla\eta^{n+1}\|^2\|\nabla u_r^{n+1}\|^2 + C\nu\Delta t\|\nabla\eta^{n+1}\|^2 + C\nu^{-1}\Delta t\|p^{n+1} - q_h\|^2 \\ &\quad+ 2C_I^2\beta_1\Delta t\mu\|\eta^{n+1}\|^2, \end{aligned} \tag{3.22}$$

where C is a generic constant which is independent of ν, p, u, T, H, C_I. Next, we bound the fourth term on the right hand side further using the ROM inverse inequality (2.9), and the stability result from Lemma 3.3

$$C\Delta t\nu^{-1}{C_b}^2\|\nabla\eta^{n+1}\|^2\|\nabla u_r^{n+1}\|^2 \leq CC_{data}\Delta t\nu^{-1}{C_b}^2|||\mathbb{S}_r|||_2\|\nabla\eta^{n+1}\|^2. \tag{3.23}$$

Now applying Lemma 2.13, using our regularity assumptions to bound the terms $\|\nabla u^{n+1}\|^2$ and $\|u_{tt}\|^2_{L^2(t_n,t_{n+1};L^2(\Omega))}$, taking q_h to be the nodal interpolant of p^{n+1}, and $\lambda := \min\{C_P^{-2}\alpha_1, \alpha_2\}$ in (3.22), it then follows that

$$\begin{aligned} &(1+2\lambda\Delta t)\|\phi_r^{n+1}\|^2 \\ &\quad\leq \|\phi_r^n\|^2 + C\nu^{-1}\Delta t^3 + C\nu^{-1}\Delta t h^{2k} + 2C_I^2\beta_1\Delta t\mu\left(h^{2k+2} + \Delta t^4 + \sum_{j=r+1}^{d}\lambda_j\right) \\ &\quad+ \Delta t(C\nu^{-1}{C_b}^2 + CC_{data}\nu^{-1}{C_b}^2|||\mathbb{S}_r|||_2 + C\nu)\left(h^{2k} + \Delta t^4 + \sum_{j=r+1}^{d}\|\nabla\varphi_j\|^2\lambda_j\right). \end{aligned} \tag{3.24}$$

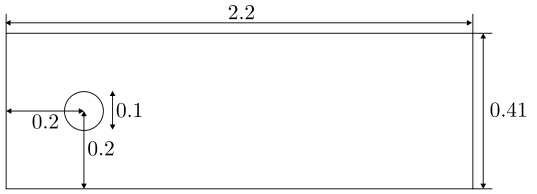

Fig. 1. Shown above is the domain for the flow past a cylinder test problem.

Finally, by Lemma 2.3, we obtain

$$\begin{aligned}\|\phi_r^{n+1}\|^2 \leq\ & \|\phi_r^0\|^2 \left(\frac{1}{1+2\lambda\Delta t}\right)^{n+1} \\ &+ 2\lambda^{-1}\Delta t^{-1}\left\{ C\nu^{-1}\Delta t^3 + C\nu^{-1}\Delta t h^{2k} + 2\beta_1 C_I^2 \Delta t\mu\left(h^{2k+2} + \Delta t^4 + \sum_{j=r+1}^{d}\lambda_j\right)\right. \\ &\left.+\ \Delta t(C\nu^{-1}C_b{}^2 + CC_{data}\nu^{-1}C_b{}^2|||\mathbb{S}_r|||_2 + C\nu)\left(h^{2k} + \Delta t^4 + \sum_{j=r+1}^{d}\|\nabla\varphi_j\|^2\lambda_j\right)\right\}.\end{aligned} \tag{3.25}$$

The triangle inequality completes the proof. □

4. Numerical experiments

In this section, we perform a numerical investigation of the new DA-ROM. In Section 4.1, we illustrate the theoretical scalings proved in Section 3. In Section 4.2, we investigate the numerical accuracy of the new DA-ROM. In Section 4.3, we investigate the new DA-ROM when inaccurate snapshots are used in its construction. Finally, in Section 4.4, we propose and investigate an adaptive nudging procedure.

For our numerical tests, we use the BDF2 analogue of (3.1): Given $u_r^0, u_r^1 \in X_r$, for $n = 1, 2, 3, \ldots$, find $u_r^{n+1} \in X_r$ such that for all $v_r \in X_r$,

$$\begin{aligned}\frac{1}{2\Delta t}(3u_r^{n+1} - 4u_r^n + u_r^{n-1}, v_r) + b^*(u_r^{n+1}, u_r^{n+1}, v_r) + \nu(\nabla u_r^{n+1}, \nabla v_r) \\ + \mu(I_H(u_r^{n+1} - u(t^{n+1})), I_H v_r) = (f^{n+1}, v_r).\end{aligned} \tag{4.1}$$

We apply (4.1) to 2D channel flow past a cylinder [41], with Reynolds number $Re = 500$. The domain is the rectangular channel $[0, 2.2]\times[0, 0.41]$, with a cylinder centered at $(0.2, 0.2)$ and radius 0.05, see Fig. 1. There is no external forcing ($f = 0$), no-slip boundary conditions are prescribed for the walls and the cylinder, and an inflow profile is given by

$$\begin{aligned}u_1(0, y, t) = u_1(2.2, y, t) &= \frac{6}{0.41^2}y(0.41 - y), \\ u_2(0, y, t) = u_2(2.2, y, t) &= 0.\end{aligned}$$

We take $\nu = 0.0002$, and enforce the zero-traction boundary condition with the usual 'do-nothing' condition at the outflow.

The DNS is run to $t = 15$ with the usual BDF2-FEM discretization [39] using (P_2, P_1^{disc}) Scott–Vogelius elements on a barycenter refined Delaunay mesh that provided 103K velocity dof, a time step of $\Delta t = 0.002$, and with the simulations starting from rest ($v_h^0 = v_h^1 = 0$). Lift and drag calculations were performed for the computed solution and compared to the literature [41,42], which verified the accuracy of the DNS. To generate the ROM basis, we used one period of snapshot data (0.28 s, or 140 time steps), starting at t = 5; by t = 5, the solution had reached a periodic-in-time state.

For the calculations of lift and drag, we used the global integral formulation from [43], where a pressure is not necessary if the test functions are chosen appropriately in the discretely divergence free space V_h.

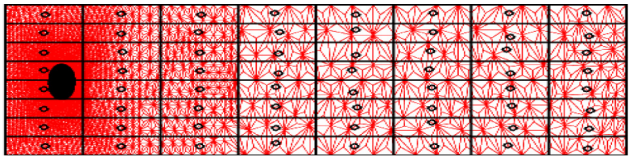

Fig. 2. Shown above is a FE mesh (in red) and the $H = \frac{2.2}{8}$ coarse mesh and nodes (in black). (For interpretation of the references to color in this figure legend, the reader is referred to the web version of this article.)

Table 1
DA-ROM rates of convergence with respect to the ROM truncation.

No. modes	$(\sum_{j=r+1}^{d} \lambda_j(1+\|\nabla\varphi_j\|^2))^{1/2}$	Error	Rate
8	2.218e+2	4.980e−2	–
10	1.077e+2	4.850e−2	1.74
12	9.246e+1	3.046e−2	2.51
14	7.680e+1	1.793e−2	1.70
16	4.590e+1	1.360e−2	1.36
18	3.334e+1	9.498e−3	1.12
20	2.601e+1	6.974e−3	1.24

The coarse mesh for DA is constructed using the intersection of a uniform rectangular mesh with the domain. We take H to be the width of each rectangle, and use $H = \frac{2.2}{20}$ (400 measurement locations) in our tests. Fig. 2 shows in red a 35K dof mesh and associated $H = \frac{2.2}{8}$ coarse mesh in black.

For the DA-ROM computations, we start from zero initial conditions $v_h^1 = v_h^0 = 0$, use the same spatial and temporal discretization parameters as the DNS, and start assimilation with the $t = 5$ DNS solution (i.e., time 0 for DA-ROM corresponds to $t = 5$ for the DNS).

4.1. Rates of convergence

In this section, we illustrate numerically the rates of convergence in Section 3. Theorem 3.5 gave a DA-ROM error estimate that depends on the ROM eigenvalues and eigenfunctions, for sufficiently large n and assumptions on μ and H:

$$\|u^{n+1} - u_r^{n+1}\| \leq C(\nu)\left(\Delta t^2 + h^{k+1} + \left(\sum_{j=r+1}^{d} \lambda_j(1+\|\nabla\varphi_j\|^2)\right)^{1/2}\right),$$

where (λ_j, φ_j) are the eigenpairs of the ROM eigenvalue problem described in Section 2.1. Table 1 illustrates the dependence of the error bound on the dimension of the DA-ROM space, r. Taking $\mu = 100$, $H = \frac{2.2}{20}$, $Re = 500$, we run the ROM with varying r and calculate the L^2 spatial error at $t = 1$. We also calculate the quantity in the error estimate corresponding to the eigenvalues and eigenfunctions (i.e., $\sum_{j=r+1}^{d} \lambda_j(1+\|\nabla\varphi_j\|^2))^{1/2}$), and use this and the error to calculate the corresponding convergence rate with respect to increasing r. From the theorem, we expect a rate of 1, and our results are consistent with this rate.

4.2. Numerical accuracy

In this section, we investigate the numerical accuracy of the new DA-ROM. Specifically, we compare the performance of the DA-ROM to that of the standard ROM ($\mu = 0$) and the DNS solution in predicting energy, drag, and lift. We run to t = 15, and run tests with both $N = 8$ and $N = 16$ modes, with varying μ, and for $Re = 500$ and 1000. Results for energy and drag prediction are shown in Fig. 3 for $Re = 500$ and Fig. 4 for $Re = 1000$, and in Tables 2–3 for error to DNS, and max lift and drag prediction. A clear improvement is observed in all cases for using DA, with $\mu = 500$ giving the best, or close to best, prediction in every case, but from the tables we observe similar accuracy for $\mu = 100,\ 500,\ 1000$. The standard ROM ($\mu = 0$) and small nudging $\mu = 1,\ 10$ are

Table 2
$L^2(10, 15; L^2(\Omega))$ error, max lift and drag on [2,11], and errors from the computed reference solution (reference max lift = 2.96520, reference max drag = 3.48329), for varying μ, $N = 8$ and 16, and $Re = 500$.

$Re = 500$					
μ	$\|u - u_r\|_{L^2(10,15;L^2)}$	c_l^{max}	$\|error\|$	c_d^{max}	$\|error\|$
	$N = 8$				
0	3.280e−1	3.150	1.848e−1	3.879	3.955e−1
1	3.216e−1	3.148	1.824e−1	3.874	3.911e−1
10	2.716e−1	3.128	1.623e−1	3.840	3.568e−1
50	1.560e−1	3.068	1.025e−1	3.739	2.559e−1
100	1.163e−1	3.022	5.626e−2	3.662	1.791e−1
500	9.638e−2	2.933	3.223e−2	3.490	6.739e−3
1000	9.976e−2	2.926	3.903e−2	3.433	5.068e−2
	$N = 16$				
0	9.838e−2	2.9969	3.171e−2	3.553	6.9200e−2
1	9.835e−2	2.9957	3.070e−2	3.551	6.736e−2
10	9.770e−2	2.9856	2.039e−2	3.535	5.190e−2
50	8.863e−2	2.9564	8.611e−2	3.491	7.703e−2
100	7.330e−2	2.9374	2.784e−2	3.463	2.075e−2
500	4.594e−2	2.9083	5.694e−2	3.413	7.029e−2
1000	6.456e−2	2.9109	5.409e−2	3.394	8.936e−2

Table 3
$L^2(10, 15; L^2(\Omega))$ error, max lift and drag on [2,11], and errors from the computed reference solution (reference max lift = 3.19080, reference max drag = 3.71098), for varying μ, $N = 8$ and 16, and $Re = 1000$.

$Re = 1000$					
μ	$\|u - u_r\|_{L^2(10,15;L^2)}$	c_l^{max}	$\|error\|$	c_d^{max}	$\|error\|$
	$N = 8$				
0	3.546e−1	3.656	4.652e−1	4.665	9.540e−1
1	3.515e−1	3.649	4.652e−1	4.651	9.400e−1
10	3.230e−1	3.597	4.062e−1	4.536	8.250e−1
50	2.183e−1	3.437	2.459e−1	4.205	4.945e−1
100	1.514e−1	3.337	1.462e−1	4.015	3.040e−1
500	1.273e−1	3.191	2.020e−4	3.749	3.820e−2
1000	1.391e−1	3.183	7.407e−3	3.703	8.192e−3
	$N = 16$				
0	6.697e−1	2.956	2.344e−1	3.260	4.509e−1
1	6.619e−1	2.957	2.337e−1	3.262	4.492e−1
10	5.944e−1	2.965	2.259e−1	3.279	4.317e−1
50	3.647e−1	3.001	1.903e−1	3.357	3.543e−1
100	2.137e−1	3.036	1.550e−1	3.435	2.762e−1
500	8.135e−2	3.106	8.498e−2	3.599	1.124e−1
1000	9.137e−2	3.126	6.460e−2	3.619	9.182e−1

significantly less accurate. The effect of DA on accuracy is similar for both choices of N, and for both choices of Re.

4.3. Inaccurate snapshots

In this section, we investigate the DA-ROM performance when the snapshots are inaccurate. Specifically, we consider the same test as in Section 4.2, but now with only a small amount of data being used to build the ROM basis. This is an important aspect of the ROM to investigate, because in practical applications complete data is

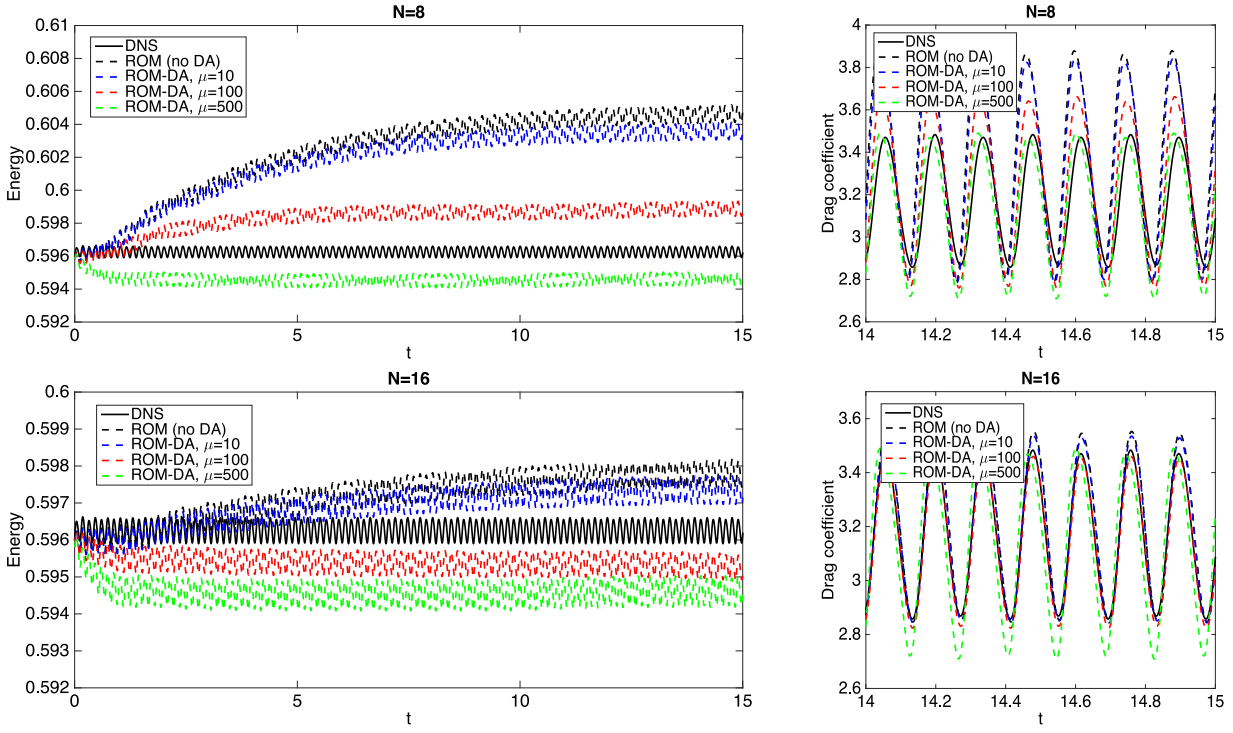

Fig. 3. Shown above are energy and drag coefficient versus time, for $Re = 500$ DA-ROM with different choices of μ, $H = \frac{2.2}{20}$, and with 8 modes (top) and 16 modes (bottom).

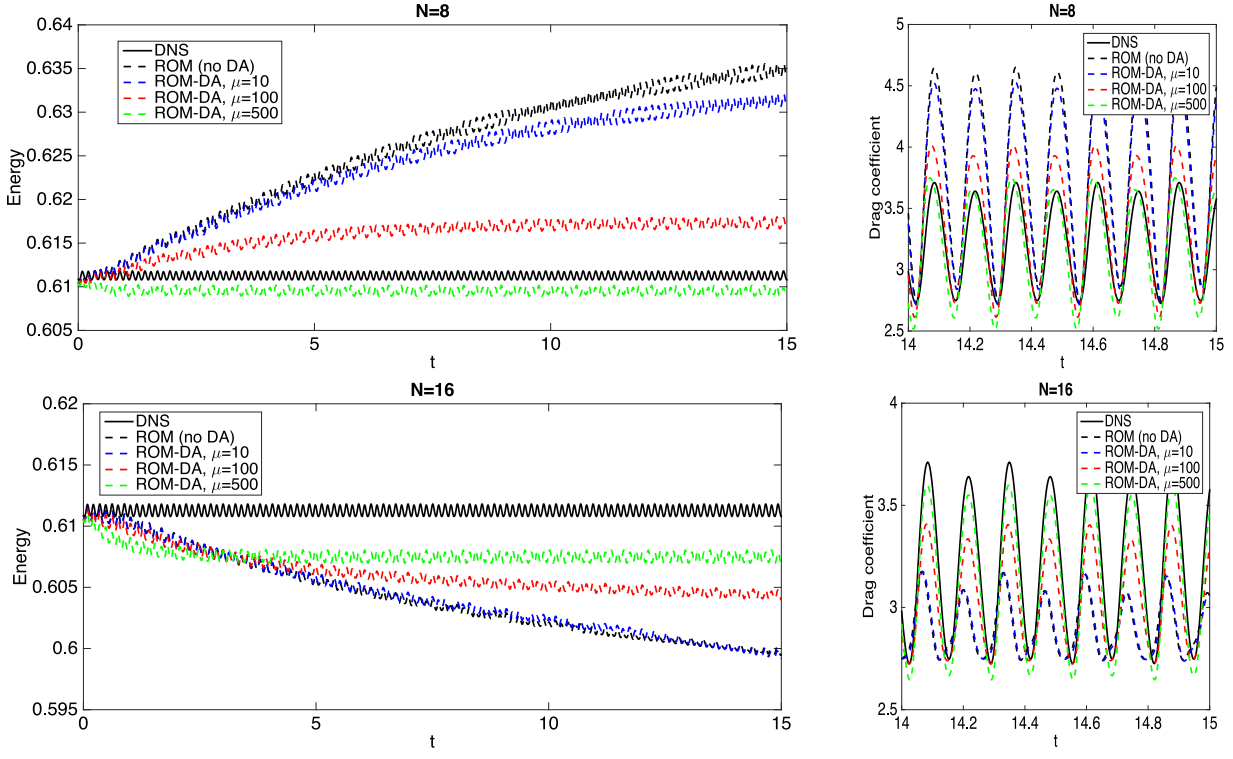

Fig. 4. Shown above are energy and drag coefficient versus time, for $Re = 1000$ DA-ROM with different choices of μ, $H = \frac{2.2}{20}$, and with 8 modes (top) and 16 modes (bottom).

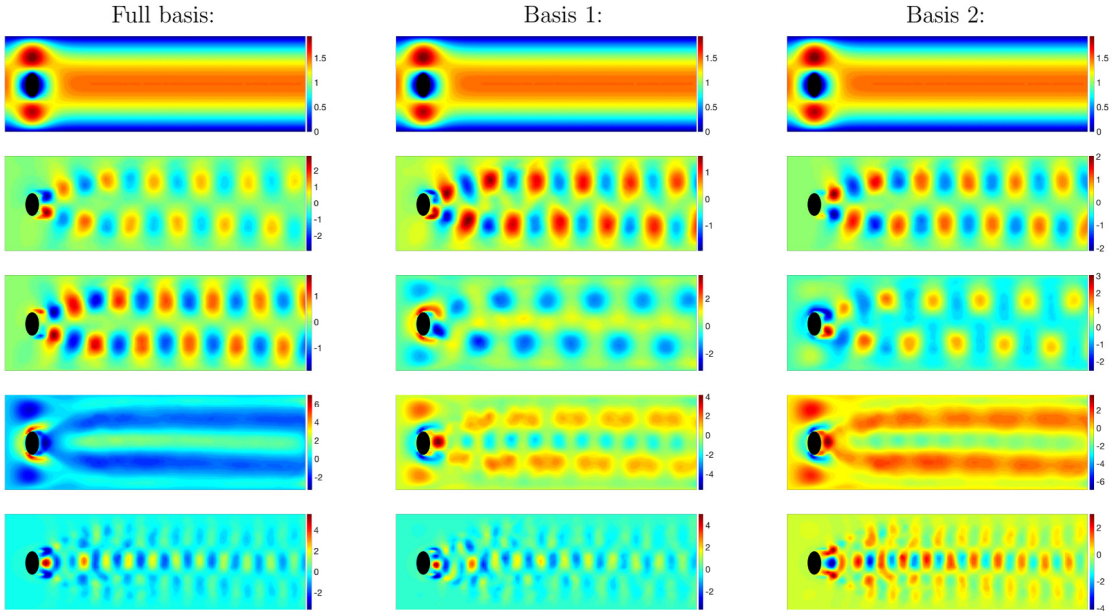

Fig. 5. Pictured above are the first 5 basis functions generated by the ROM for first the full basis, then inaccurate bases 1 and 2, which both use less than one period of data to generate the basis.

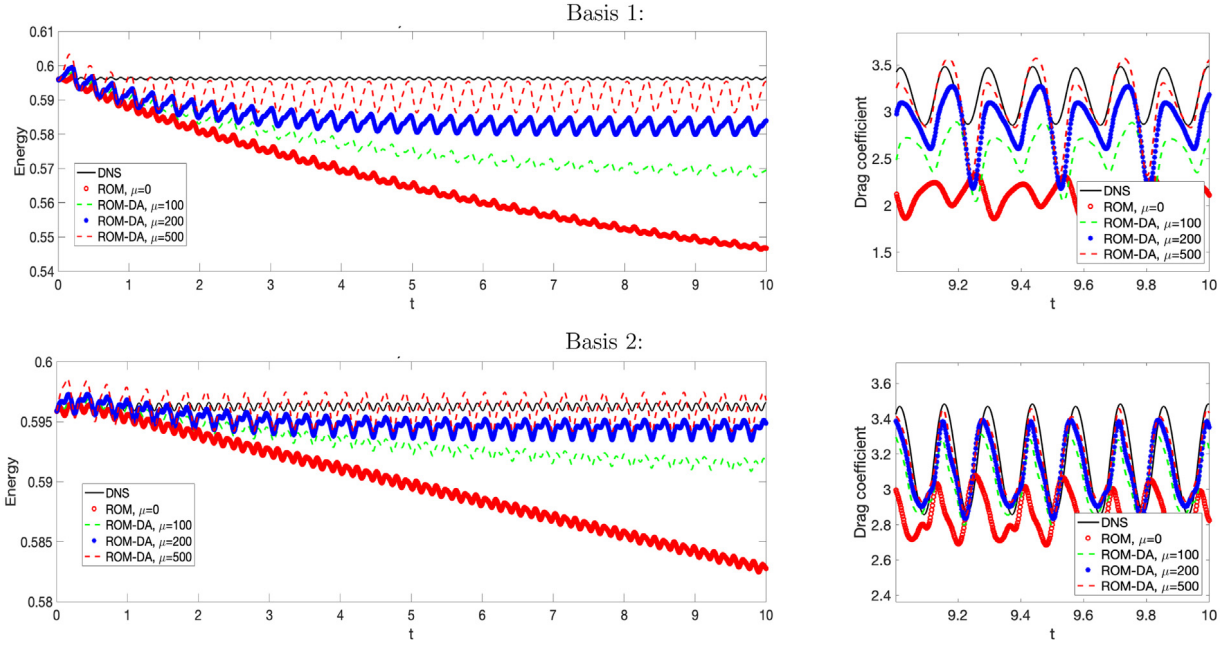

Fig. 6. Energy and drag coefficient versus time plots with different values of μ for $Re = 500$ using 8 modes and $H = \frac{2.2}{20}$.

generally not available, or the amount of data needed to sufficiently capture the behavior of the true solution is unknown.

We generated these inaccurate snapshots for $Re = 500$ using less than one period of data: basis 1 used 64% of one period of DNS data (the first 90 time step solutions from the 140 which comprise a full period, starting at

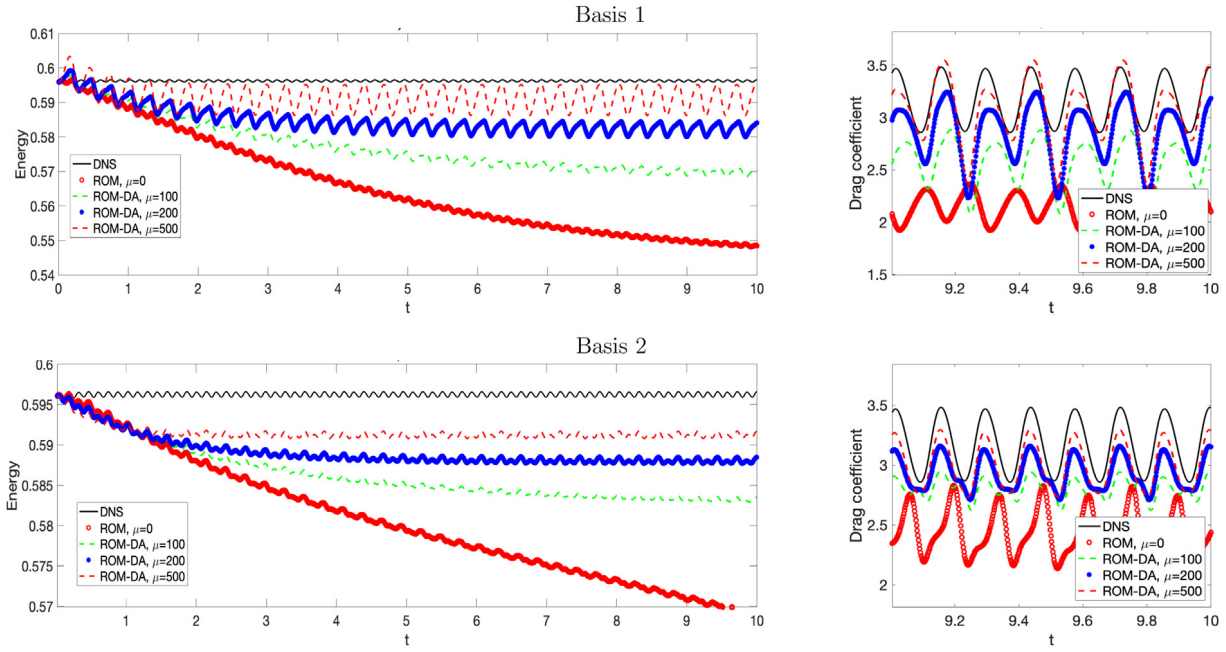

Fig. 7. Energy and drag coefficient versus time plots with different values of μ for $Re = 500$ using 12 modes and $H = \frac{2.2}{20}$.

t = 5) while basis 2 used 84% (the first 120 time step solutions). See Fig. 5 for the first five basis functions generated by the ROM; the basis functions for the full ROM are also included for comparison.

In Fig. 6, we show the results of the DA-ROM using only 8 modes, with basis 1 and 2 defined above, and μ ranging from 100 to 500. DA significantly improves the accuracy of the ROM, and basis 2 does better at predicting the drag coefficient than basis 1.

Fig. 7 shows energy and drag coefficient plots versus time using $N = 12$ modes, and the nudging parameter μ is varied from 100 to 500. We see similar results as the case of using 8 modes; for both bases, DA significantly improves the accuracy of the ROM, compared to the ROM without DA ($\mu = 0$), which becomes more and more inaccurate as time goes on. Basis 2 is able to accurately predict the drag coefficient.

The results in this section suggest that DA can dramatically improve the accuracy of a ROM when insufficient data is available to build the ROM, which is the general case in practical applications. We also emphasize that the improvement in the DA-ROM accuracy over the standard ROM accuracy is significantly larger in the realistic case of inaccurate snapshot construction. Indeed, comparing Figs. 6 and 7 with Fig. 3, we notice that the absolute improvement in the DA-ROM is much larger in the former than in the latter (this could be clearly seen from the magnitude of the y-axis).

4.4. Adaptive nudging

To further improve the accuracy of the DA-ROM solution, we also consider nudging that is adaptive in time. While the error estimate we prove guarantees convergence up to discretization error and ROM truncation error exponentially fast in time, it may not be sufficient to expect good numerical results. In practice, the ROM truncation error is often quite large, and can make the error bounds be too large to guarantee accurate predictions, especially over long time intervals. We propose below an adaptive nudging technique that will help produce better results by forcing the DA-ROM predicted energy to be more accurate.

To our knowledge, the ideas below for adaptive nudging in time are new, and moreover they are not restricted to the ROM setting. The authors plan to consider this in a general setting, and in much more depth, in a forthcoming work where the ideas are explored both analytically and numerically, and considering sensitivity with respect to parameters.

4.4.1. Algorithm

In this section, we propose to change μ adaptively in time, based on the accuracy of the energy prediction of the ROM as well as the sign of the contribution of the DA term to the energy balance. The semi-discrete algorithm reads: Find $u_r \in X_r$ such that for all $v_r \in X_r$,

$$((u_r)_t, v_r) + b^*(u_r, u_r, v_r) + \nu(\nabla u_r, \nabla v_r) + \mu(I_H(u_r - u), I_H v_r) = (f, v_r), \tag{4.2}$$

with $v_0 = P_r(u_0)$, and μ is the adaptive nudging parameter.

We begin the discussion with an energy estimate. Choosing $v_r = u_r$ vanishes the nonlinear term, and after bounding the forcing term in the usual way we obtain the energy estimate

$$\frac{d}{dt}\|u_r\|^2 + \nu\|\nabla u_r\|^2 + \mu\left(\|I_H(u_r)\|^2 - \|I_H(u)\|^2 + \|I_H(u_r - u)\|^2\right) \leq \nu^{-1}\|f\|_{-1}.$$

We assume this estimate is sharp in the following analysis, and that we know $\|u(t^n)\|$ in addition to $I_H(u)(t^n)$. Needing to know the kinetic energy at every time step may be an obstacle to using adaptive nudging, but if H is sufficiently small, then approximating $\|u(t^n)\|$ with $\|I_H(u)(t^n)\|$ could be a workaround in practice. We will consider this issue in more detail in a forthcoming work.

The adaptive strategy is to adjust μ so the contribution of the data assimilation term removes dissipation if the ROM-DA energy is too small, and adds dissipation if the energy is too large. We use the term dissipation loosely, since here we refer to dissipation from the DA term only meaning that it adds positivity to the left hand side of the energy estimate. Now after step n we can calculate (1) the DA-ROM energy $\frac{1}{2}\|u_r^n\|^2$ and the true energy $\frac{1}{2}\|u(t^n)\|^2$; and (2) the sign of the contribution of the data assimilation term (DAT):

$$DAT := \|I_H(u_r)(t^n)\|^2 - \|I_H(u)(t^n)\|^2 + \|I_H(u_r - u)(t^n)\|^2.$$

With this information, we check the energy error to see if it is too high (or too low), and if so, then add dissipation by increasing μ if $DAT > 0$ and decreasing μ otherwise; or do the opposite to decrease dissipation.

Algorithm 4.1 (*DA-ROM with Adaptive Nudging*)**.**

1. Initialize problem variables and parameters for (4.1).
2. Define L to be the frequency in number of time steps to adapt μ.
3. Define δ_μ to be the adjustment size to use for changing μ.
4. Define tol to be the tolerance for making a change to μ.
5. For time step $n = 1, 2, \ldots$
   if mod(n,L)==0
   (a) Calculate DAT$= \|I_H(u_r)(t^n)\|^2 - \|I_H(u)(t^n)\|^2 + \|I_H(u_r - u)(t^n)\|^2$
   and $E_{diff} = \frac{1}{2}\left(\|u_r(t^n)\|^2 - \|u(t^n)\|^2\right)$
   (b) if ($E_{diff} > tol$ and DAT> 0) or ($E_{diff} < -tol$ and DAT< 0)
   Set $\mu = \mu + \delta_\mu$.
   if ($E_{diff} < -tol$ and DAT> 0) or ($E_{diff} > tol$ and DAT< 0)
   Set $\mu = \mu - \delta_\mu$.
   end
   Calculate $u_r(t^{n+1})$ from (4.1).

How to select good L, δ_μ, and tol are interesting and important questions. In our numerical tests below, we used $L = 10$, $tol = 10^{-3}$, and $\delta_\mu = 1$ for the plots, but also varied the parameters to give some preliminary testing of parameter sensitivity. We intend to explore sensitivity more in depth for adaptive nudging in a forthcoming paper.

4.4.2. Numerical results

We follow the same problem setup outlined in Section 4.2, using $Re = 1000$, again using the full ROM basis with $N = 8$ modes, but now choosing μ adaptively in time. Fig. 8 shows the energy plot for the DA-ROM algorithm with the adaptive nudging ($L = 10$, $tol = 1e-3$, $\delta_\mu = 1$, starting $\mu = 100$), and compares with DNS, standard ROM (DA-ROM with $\mu = 0$), and DA-ROM with constant $\mu = 100$. We observe the adaptive nudging has a positive effect on energy error, slowly reducing the error and causing the adaptive DA-ROM energy to almost coincide

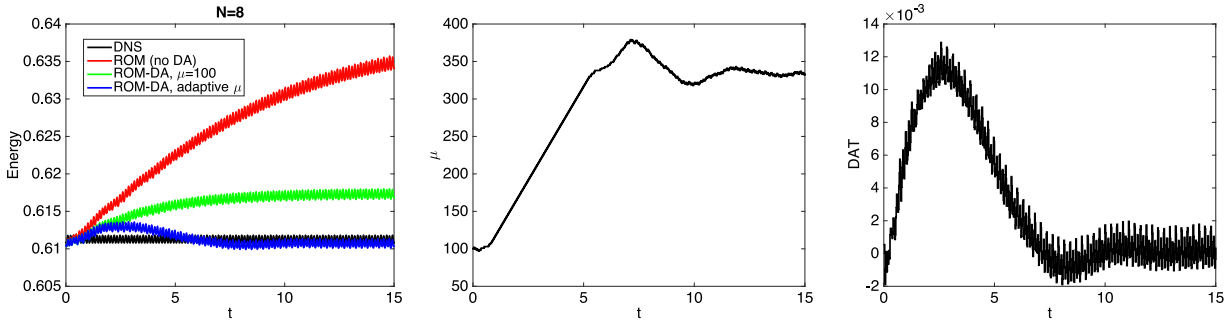

Fig. 8. Energy, μ, and DAT versus time, for $Re = 1000$ DA-ROM with $N = 8$ and and $H = \frac{2.2}{20}$, using different choices of μ (adaptive used $L = 10$, $tol = 1e-3$, $\delta_\mu = 1$), with $N = 8$ modes and $H = \frac{2.2}{20}$.

Table 4
$L^2(10, 15; L^2(\Omega))$ and energy error for varying starting μ, tol, L, δ_μ, for DA-ROM with adaptive nudging, using $N = 8$ and $Re = 1000$.

Starting μ	tol	L	δ_μ	Final μ	$\|u - u_r\|_{L^2(10,15;L^2)}$	Energy error at t=15
100	1e−2	10	1	239	1.201e−1	8.868e−4
100	1e−3	10	1	333	1.217e−1	4.499e−4
100	1e−4	10	1	334	1.218e−1	5.543e−4
100	1e−2	20	5	250	1.200e−1	6.857e−4
100	1e−3	20	5	340	1.218e−1	4.421e−4
100	1e−4	20	5	330	1.218e−1	4.782e−4
100	1e−3	50	1	244	1.224e−1	1.150e−3
100	1e−3	50	5	350	1.218e−1	5.135e−4
100	1e−3	50	10	350	1.217e−1	4.546e−4
10	1e−2	10	1	267	1.202e−1	4.098e−4
10	1e−3	10	1	333	1.217e−1	4.499e−4
10	1e−2	50	5	270	1.203e−1	3.636e−4
500	1e−2	10	1	500	1.273e−1	1.636e−3
500	1e−3	10	1	334	1.218e−1	4.627e−4
500	1e−3	50	5	345	1.218e−1	4.826e−4

with the DNS energy. Plots in the figure also show the adaptive μ versus time, and DAT versus time; by t = 10, both appear to have leveled off. To test the sensitivity of the adaptive nudging parameters, we tested with varying parameters, and results are given in Table 4, as $L^2(10, 15; L^2(\Omega))$ error, the final μ, and the energy error at the final time.

When $tol \leq 1e-3$, we observe very little sensitivity in the results for any change of the other parameters. For $tol = 1e-2$, the energy errors were slightly larger and the final μ varied somewhat from the value around 350 that was found with smaller tol (smaller for small starting μ, larger for large starting μ), likely because this tolerance provided less opportunity for μ to adapt.

5. Conclusions

In this paper, we put forth a new data assimilation reduced order model (DA-ROM) for fluid flows. The new DA-ROM adds to the standard ROM a feedback control term that nudges the ROM approximation towards the reference solution corresponding to the observed data. The new DA-ROM's implementation is extremely simple. The nudging term can be implemented into existing codes completely at the linear algebraic level, without any changes to the rest of the discretization. The nudging term dramatically increases the accuracy of the new DA-ROM by utilizing the available low-resolution data, without the need to increase the number of ROM basis functions. We proved that with a properly chosen nudging parameter, the new DA-ROM algorithm converges exponentially fast in time to the true solution, up to discretization and ROM truncation errors. We also proposed a strategy for nudging adaptively in time, by adding or removing dissipation arising from the nudging to better match true solution energy.

Finally, we performed a numerical investigation of the new DA-ROM in the simulation of a 2D flow past a circular cylinder. The numerical results showed that the adaptive nudging DA-ROM significantly improves the long time ROM accuracy, especially when the snapshots used to construct the ROM are inaccurate, which is generally the case in realistic applications.

We intend to pursue several research avenues. First, we will investigate whether numerical analysis can help determine the optimal parameter in the adaptive nudging approach for the new DA-ROM. We also want to extend the numerical investigation of the DA-ROM to complex 3D flows. Finally, we will examine whether using a spectral type of nudging in the DA-ROM instead of the current physical nudging yields better results.

Acknowledgments

We thank the two reviewers for the comments and suggestions that helped improve the paper.

References

[1] J.S. Hesthaven, G. Rozza, B. Stamm, Certified Reduced Basis Methods for Parametrized Partial Differential Equations, Springer, 2015.
[2] P. Holmes, J.L. Lumley, G. Berkooz, Turbulence, Coherent Structures, Dynamical Systems and Symmetry, Cambridge, 1996.
[3] A. Quarteroni, A. Manzoni, F. Negri, Reduced Basis Methods for Partial Differential Equations: An Introduction, Vol. 92, Springer, 2015.
[4] M. Benosman, J. Borggaard, O. San, B. Kramer, Learning-based robust stabilization for reduced-order models of 2D and 3D Boussinesq equations, Appl. Math. Model. 49 (2017) 162–181.
[5] J. Östh, B.R. Noack, S. Krajnović, D. Barros, J. Borée, On the need for a nonlinear subscale turbulence term in POD models as exemplified for a high-Reynolds-number flow over an Ahmed body, J. Fluid Mech. 747 (2014) 518–544.
[6] B. Protas, B.R. Noack, J. Östh, Optimal nonlinear eddy viscosity in Galerkin models of turbulent flows, J. Fluid Mech. 766 (2015) 337–367.
[7] O. San, T. Iliescu, A stabilized proper orthogonal decomposition reduced-order model for large scale quasigeostrophic ocean circulation, Adv. Comput. Math. (2015) 1289–1319.
[8] K. Carlberg, M. Barone, H. Antil, Galerkin v. least-squares Petrov–Galerkin projection in nonlinear model reduction, J. Comput. Phys. 330 (2017) 693–734.
[9] M. Gunzburger, T. Iliescu, M. Schneier, A Leray regularized ensemble-proper orthogonal decomposition method for parameterized convection-dominated flows, IMA J. Numer. Anal. (2019) https://doi.org/10.1093/imanum/dry094.
[10] B. Peherstorfer, K. Willcox, Data-driven operator inference for nonintrusive projection-based model reduction, Comput. Methods Appl. Mech. Engrg. 306 (2016) 196–215.
[11] B. Galletti, C.H. Bruneau, L. Zannetti, A. Iollo, Low-order modelling of laminar flow regimes past a confined square cylinder, J. Fluid Mech. 503 (2004) 161–170.
[12] M.J. Balajewicz, I. Tezaur, E.H. Dowell, Minimal subspace rotation on the Stiefel manifold for stabilization and enhancement of projection-based reduced order models for the compressible Navier–Stokes equations, J. Comput. Phys. 321 (2016) 224–241.
[13] C.W. Rowley, T. Colonius, R.M. Murray, Model reduction for compressible flows using POD and Galerkin projection, Physica D 189 (1) (2004) 115–129.
[14] O. San, J. Borggaard, Principal interval decomposition framework for POD reduced-order modeling of convective Boussinesq flows, Internat. J. Numer. Methods Fluids 78 (1) (2015) 37–62.
[15] X. Xie, P.J. Nolan, S.D. Ross, T. Iliescu, Lagrangian data-driven reduced order modeling of finite time Lyapunov exponents. 2018. available as arXiv preprint, http://arxiv.org/abs/1808.05635.
[16] M. Mohebujjaman, L.G. Rebholz, T. Iliescu, Physically-constrained data-driven correction for reduced order modeling of fluid flows, Internat. J. Numer. Methods Fluids 89 (3) (2019) 103–122.
[17] M. Mohebujjaman, L.G. Rebholz, X. Xie, T. Iliescu, Energy balance and mass conservation in reduced order models of fluid flows, J. Comput. Phys. 346 (2017) 262–277.
[18] A. Azouani, E. Olson, E.S. Titi, Continuous data assimilation using general interpolant observables, J. Nonlinear Sci. 24 (2) (2014) 277–304.
[19] E. Kalnay, Atmospheric Modeling, Data Assimilation, and Predictability, Cambridge Univ Pr, 2003.
[20] A. Biswas, V.R. Martinez, Higher-order synchronization for a data assimilation algorithm for the 2D Navier–Stokes equations, Nonlinear Anal. RWA 35 (2017) 132–157.
[21] H. Bessaih, E. Olson, E.S. Titi, Continuous data assimilation with stochastically noisy data, Nonlinearity 28 (3) (2015) 729–753.
[22] A. Farhat, E. Lunasin, E.S. Titi, Abridged continuous data assimilation for the 2D Navier–Stokes equations utilizing measurements of only one component of the velocity field, J. Math. Fluid Mech. 18 (1) (2016) 1–23.
[23] A. Larios, L. Rebholz, C. Zerfas, Global in time stability and accuracy of IMEX-FEM data assimilation schemes for Navier–Stokes equations, Comput. Methods Appl. Mech. Engrg. 345 (2019) 1077–1093.
[24] A. Farhat, M.S. Jolly, E.S. Titi, Continuous data assimilation for the 2D Bénard convection through velocity measurements alone, Physica D 303 (2015) 59–66.
[25] P.A. Markowich, E.S. Titi, S. Trabelsi, Continuous data assimilation for the three-dimensional Brinkman–Forchheimer-extended Darcy model, Nonlinearity 29 (4) (2016) 1292.

[26] M.S. Jolly, V.R. Martinez, E.S. Titi, A data assimilation algorithm for the subcritical surface quasi-geostrophic equation, Adv. Nonlinear Stud. 17 (1) (2017) 167–192.
[27] A. Larios, Y. Pei, Nonlinear Continuous Data Assimilation, 2017, arXiv e-prints, arXiv:170303546.
[28] Y. Cao, J. Zhu, I.M. Navon, Z. Luo, A reduced-order approach to four-dimensional variational data assimilation using proper orthogonal decomposition, Internat. J. Numer. Methods Fluids 53 (10) (2007) 1571–1583.
[29] M. Kaercher, S. Boyaval, M.A. Grepl, K. Veroy, Reduced basis approximation and a posteriori error bounds for 4d-var data assimilation, Optim. Eng. (2018) 1–33.
[30] Y. Maday, A.T. Patera, J.D. Penn, M. Yano, A parameterized-background data-weak approach to variational data assimilation: formulation, analysis, and application to acoustics, Internat. J. Numer. Methods Engrg. 102 (5) (2015) 933–965.
[31] R. Ştefănescu, A. Sandu, I.M. Navon, POD/DEIM reduced-order strategies for efficient four dimensional variational data assimilation, J. Comput. Phys. 295 (2015) 569–595.
[32] V. John, Finite Element Methods for Incompressible Flow Problems, in: Springer Series in Computational Mathematics, Springer International Publishing, 2016.
[33] K. Kunisch, S. Volkwein, Galerkin proper orthogonal decomposition methods for parabolic problems, Numer. Math. 90 (1) (2001) 117–148.
[34] T. Iliescu, Z. Wang, Variational multiscale proper orthogonal decomposition: Navier-Stokes equations, Num. Meth. P.D.E.s 30 (2) (2014) 641–663.
[35] J.R. Singler, New POD error expressions, error bounds and asymptotic results for reduced order models of parabolic PDEs, SIAM J. Numer. Anal. 52 (2) (2014) 852–876.
[36] L.G. Rebholz, C. Zerfas, Simple and efficient continuous data assimilation of evolution equations via algebraic nudging. arXiv e-prints, arXiv:1810.03512, 2018.
[37] B. García-Archilla, J. Novo, Error analysis of fully discrete mixed finite element data assimilation schemes for the Navier–Stokes equation. 2019. available as arXiv preprint, https://arxiv.org/abs/1904.06113.
[38] B. García-Archilla, J. Novo, E. Titi, Uniform in time error estimates for a finite element method applied to a downscaling data assimilation algorithm for the Navier–Stokes equations. 2018. available as arXiv preprint, https://arxiv.org/abs/1807.08735.
[39] W.J. Layton, Introduction to the Numerical Analysis of Incompressible Viscous Flows, Vol. 6, Society for Industrial and Applied Mathematics (SIAM), 2008.
[40] T. Iliescu, Z. Wang, Are the snapshot difference quotients needed in the proper orthogonal decomposition? SIAM J. Sci. Comput. 36 (3) (2014) A1221–A1250.
[41] M. Schäfer, S. Turek, The benchmark problem 'flow around a cylinder' flow simulation with high performance computer II, Notes Numer. Fluid Mech. 52 (1996) 547–566.
[42] X. Xie, M. Mohebujjaman, L. Rebholz, T. Iliescu, Data-driven filtered reduced order modeling of fluid flows, SIAM J. Sci. Comput. 40 (3) (2018) B834–B857.
[43] V. John, Reference values for drag and lift of a two dimensional time-dependent flow around a cylinder, Internat. J. Numer. Methods Fluids 44 (2002) 777–788.